

Supporting Information

1 Mie scattering

Rayleigh-Debye-Gans (RDG) theory is applicable only if the electric field of the incident radiation thoroughly penetrates the particles of interest, i.e., if the magnitude of the electric field vector inside and around the particle is identical to the incident wave^[1]. If this is not the case, the scattered field has to be calculated using Mie equations^[2], which significantly complicates the situation.

Glatter^[1] writes that for the RDG theory to be applicable, the particles must not reflect the incoming light and the phase shift caused by the particles must be negligible. For this to be the case $2\alpha|m - 1| \ll 1$, where α is a parameter related to the size of the particles

$$\alpha = \frac{2\pi R}{\lambda_0} \quad (1)$$

with R the radius of the particle and λ_0 wavelength of the incident beam in vacuum, and m is the ratio of real parts of the refractive indices of the particle and solvent.

For scattering experiment with laser wavelength of 633 nm involving pure polystyrene (PS) particles in water, $m = 1.587^{[3]}/1.332 = 1.191$. Calculations by Glatter^[1] show that Mie effects for such ratio and particles with radii of several hundred nanometers would be likely observable as smearing of the form factor minima and their slight shift towards smaller q values.

In contrast to PS particles, PNIPAM microgels are hydrogel particles extensively swollen by the solvent. Stieger et al.^[4] found that the volume fraction of polymer inside PNIPAM particles in the swollen state is typically 20 % and below. We can estimate the m ratio for PNIPAM particles by a simple back of the envelope calculation. Assuming the refractive index for PNIPAM is of the same magnitude as that of poly(methylmethacrylate), $n = 1.489^{[3]}$ at 633 nm and that the refractive index of the overall particle can be described by a simple superposition, $m \approx (0.2 \cdot 1.489 + 0.8 \cdot 1.332)/1.332 = 1.024$. Given

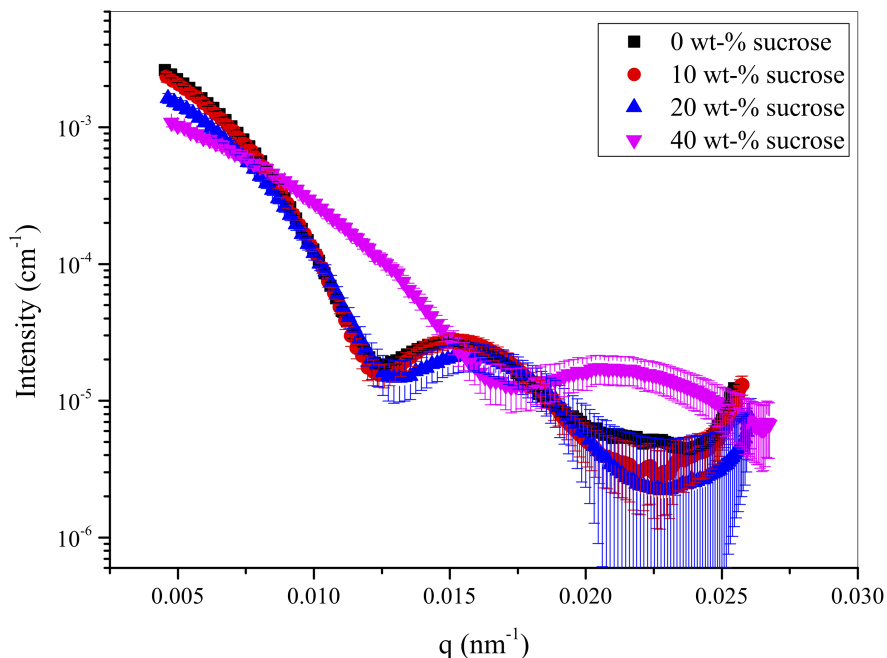


Figure 1: 7.2 mol – % KPS batch measured in water and at various sucrose concentrations at 642 nm.

that $m = 1.000$ is the ideal value for RDG regime, we expect that the Mie effects for the swollen microgels used in this work are negligible or small. Given that particle counting from scanning electron micrographs showed that the PDI of the particle radius distributions were 10 % and below, the experimentally measured form factors should have been significantly more smeared out in the case that strong Mie effects are present.

Nevertheless we attempted a contrast matching experiment with 7.2 mol – % BIS KPS particles in aqueous sucrose solutions to see whether the form factors would become less smeared when the solvent refractive index was increased, i.e. the refractive index difference between particles and solvent was made smaller.

Figure 1 shows scattered intensity from 7.2 mol – % KPS batch at various sucrose concentrations. The highest BIS content batch was chosen as reference as it is expected to have the highest polymer volume fraction and therefore exhibit the strongest Mie effects, if present. For particles with lower BIS contents, these effects would be expected to be smaller. As seen in Figure 1, the overall scattering intensity diminishes with increasing sucrose concentration, as expected for lowering contrast. The problem proves to be the fact that sucrose forces the water out of the hydrogel particles, and

consequently they shrink at high sucrose concentrations. This makes it impossible to evaluate reliably whether the form factors become sharper with diminishing contrast, even though this does not appear to be the case. Based on considerations presented here, we conclude that any Mie effects, if present, are small and do not change the overall interpretation of the results presented in this work.

2 Test cases

2.1 Introduction

The performance of the direct inversion method was evaluated by inverting artificial test datasets that simulate real world data to different degrees. All the datasets include permutations typical of a light scattering measurements, such as incorrect background subtraction (the actual background was higher than what was subtracted), shifts in laser wavelengths and dispersion refractive indices in respect to their nominal values, higher number of integration points for the particle radius distribution (150 vs 50) and the excess contrast profile (150 vs 20). In addition Gaussian PSD was used for the radius distribution function whereas Burr Type XII distribution were used for fitting. These permutations lead to wrong q values, additional background in the data and introduce a small model mismatch.

Inversion method was tested against two particle types: I) fuzzy sphere conforming to the classical notion of PNIPAM microgel structure and II) partially hollow fuzzy sphere, each with three different noise levels (scaled Poisson noise). These particle types were chosen to investigate whether the assumed characteristics of our actual samples would be detectable by the direct inversion method. Furthermore, in order to compare the suitability of different smoothing norms on these specific particle structures, all datasets were fitted with total variation and 1st and 2nd derivative smoothing norms.

For each test problem and noise level two form factors were created, one with nominal wavelength of 642 nm and another one with 404 nm. For each noise level both traces were fitted globally and the regularization parameter λ values were varied in order to find out the optimal level of filtering according to the L-curve criterion^[5].

2.2 Fuzzy sphere particles

Figure 2 shows the generated datasets, fits, solutions and the exact solution for the fuzzy sphere test problem. Typical L-curve is shown in Figure 3 (test case D in Figure 2). For all the solutions the λ value was chosen close to the L-curve corner, from the right hand side.

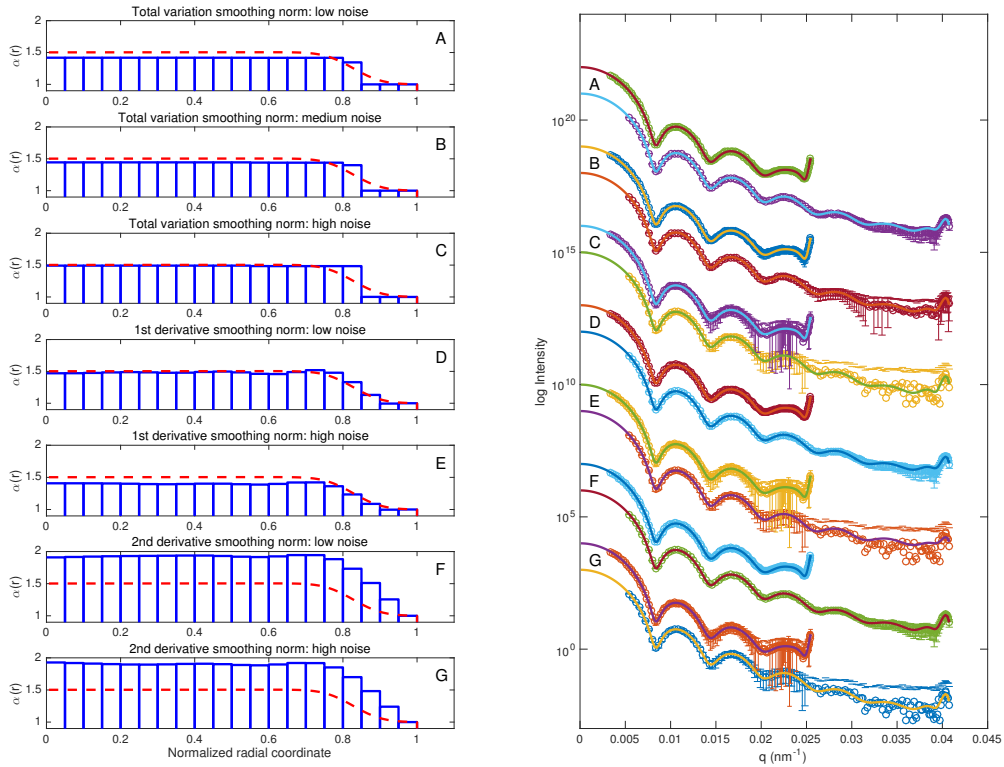


Figure 2: Solutions (left) and form factor fits (right) to the fuzzy sphere test problem. Dashed red line in the solutions denotes the exact solution that was used to create the test cases. Solid lines on the right indicate the fit function. Solutions to test cases A-C were obtained with total variation smoothing norm, D-E with 1st derivative smoothing norm and F-G with 2nd derivative smoothing norm. Relative noise levels in test cases were A: 1.7×10^{-4} and 2.3×10^{-4} , B: 6.1×10^{-4} and 6.4×10^{-4} , C: 1.9×10^{-3} and 2.8×10^{-3} , D: 1.7×10^{-4} and 2.3×10^{-4} , E: 1.9×10^{-3} and 2.8×10^{-3} , F: 1.7×10^{-4} and 2.3×10^{-4} , G: 1.9×10^{-3} and 2.8×10^{-3} .

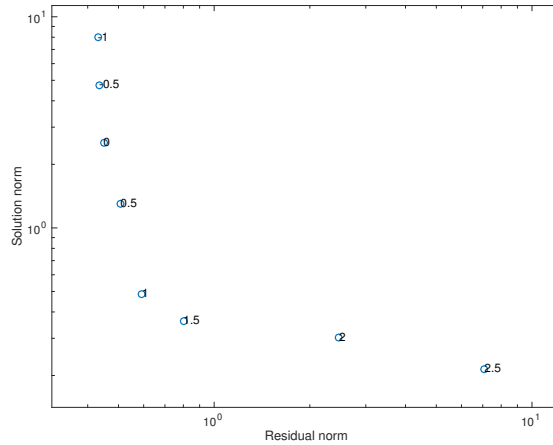


Figure 3: L-curve for test case D in Figure 2. Numbers beside the points denote the $\log \lambda$ value.

Figure 2 shows that all the smoothing norms capture the essence of the exact solution for all the used noise levels, i.e., the constant density core and low density periphery of the fuzzy particle. The details of the solutions reveal distinctive characteristics of the different smoothing norms. Total variation smoothing norm can accommodate steep gradients, and consequently the solutions are reduced to their bare minimum. Fuzzy particles appear as core-shell structure with less dense shell in comparison to the core. This simplicity of solutions is generally preferable, as the solution contains the minimum amount of features to fit the data and therefore the details of the solution are less likely to be artifacts^[6].

The first derivative smoothing norm clearly produces the most faithful reproduction of the exact solution. At low noise level the relative contrast difference between the particle core and particle periphery is estimated correctly, whereas at high noise level it is somewhat underestimated. This is understandable as the increased noise in combination with filtering gives less weight to high q data points. Fuzzy particles are characterized by the fast decay of the form factor^[4], and disregarding the high q data reduces the apparent fuzziness. Finally, the second derivative smoothing norm forces excessive smoothness, which leads to overestimation of the relative difference between the particle core and particle periphery, but nevertheless captures correctly the overall particle structure.

2.3 Partially hollow fuzzy sphere particles

Figure 4 shows the solutions and fits for the partially hollow fuzzy particle test problem. Generally this test problem proves to be more challenging for the inversion rou-

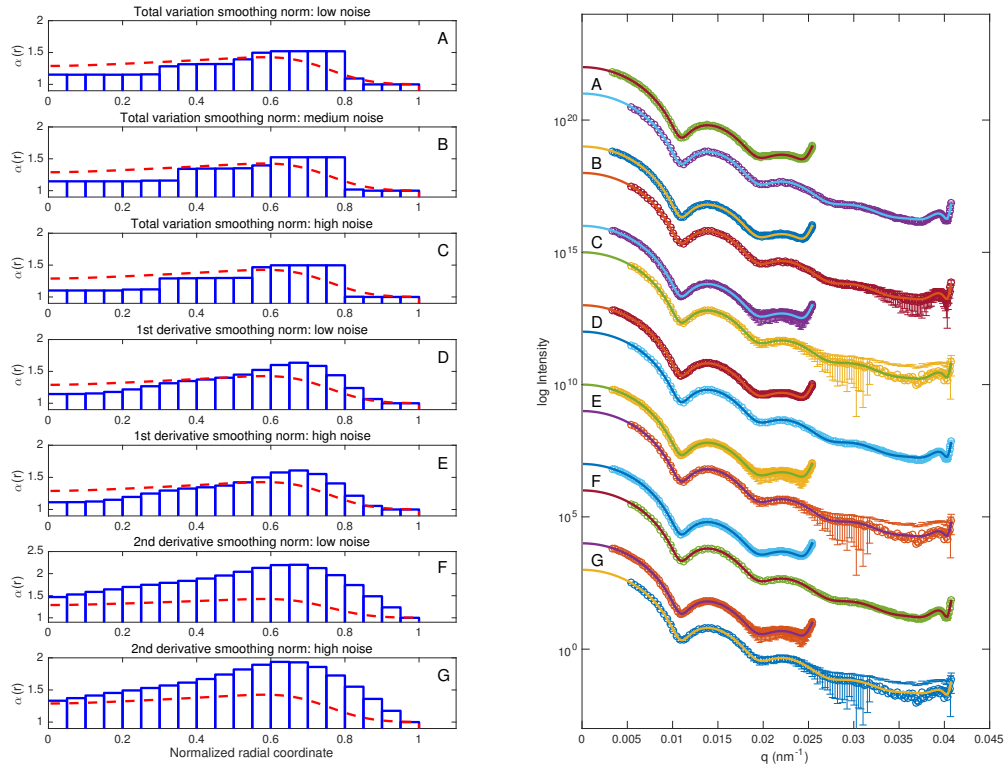


Figure 4: Solutions (left) and form factor fits (right) to the partially hollow fuzzy sphere test problem. Dashed red line in the solutions denotes the exact solution that was used to create the test cases. Solid lines on the right indicate the fit function. Solutions to test cases A-C were obtained with total variation smoothing norm, D-E with 1st derivative smoothing norm and F-G with 2nd derivative smoothing norm. Relative noise levels in test cases were A: 1.3×10^{-4} and 1.1×10^{-4} , B: 4.5×10^{-4} and 5.1×10^{-4} , C: 1.8×10^{-3} and 1.9×10^{-3} , D: 1.3×10^{-4} and 1.1×10^{-4} , E: 1.8×10^{-3} and 1.9×10^{-3} , F: 1.3×10^{-4} and 1.1×10^{-4} , G: 1.8×10^{-3} and 1.9×10^{-3} .

tine, but the main features come across for all the noise levels and smoothing norms. All the solutions tend to overestimate the relative excess contrast function at the maximum and underestimate it at the core. The second derivative smoothing norm suffers from the same problem as in the fuzzy sphere test case, i.e., the relative excess contrast function is overestimated because of insufficient flexibility due to excessive smoothing.

2.4 Conclusion

Both the test cases, fuzzy sphere and partially hollow fuzzy sphere structures, show that the direct inversion method is able to resolve the main features of this type of particles in the presence of noise and permutations. The recovered relative excess contrast functions do not necessarily provide "exact" reconstructions but are sufficient to classify particles based on main characteristics. It is clear that one should avoid the interpretation of minute details of the solutions. In this respect the total variation smoothing norm provides the best compromise between obtaining a useful reconstruction but avoiding artifacts resulting from the inversion process.

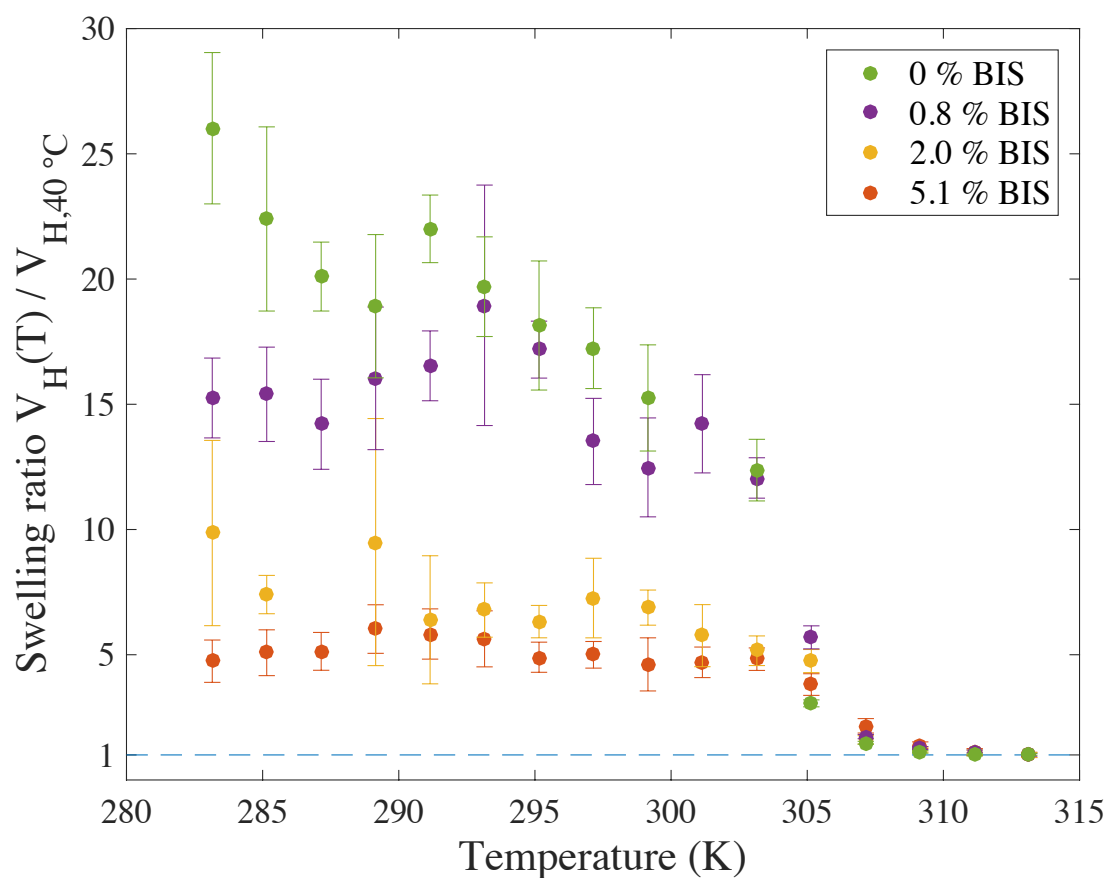


Figure 5: Volume phase transition behavior of selected KPS initiated batches.

3 Volume phase transition behavior of ultra low cross-linked particles

Figure 5 shows the volume phase transition behavior of 0, 0.8, 2.0 and 5.1 mol – % KPS initiated batches. Relatively high error in the hydrodynamic volumes of batches with low cross-linker amount is due to large swollen size and low scattering contrast at low temperatures. Regardless of cross-linker content the most rapid collapse takes place between 305 and 307 K, where PNIPAM VPTT is typically reported.^[7] The particle architecture changes from inverted to fuzzy between 0 and 2.0 mol – %, but the difference in the particle structure does not affect the VPTT behavior.

4 Is Gaussian function a good approximation for the radius distribution?

The particle nucleation phase in precipitation polymerization of NIPAM appears to be sensitive to the charge density of polymer generated under given polymerization conditions^[8], and its duration has to be short, which can be deduced from the fact that the experimentally observed particle size distributions are narrow. Consequently also no particle aggregation take place under typical reaction conditions.

The exact shape of the radius size distribution function is determined by the nucleation mechanism and the ability of different size fractions to capture material in the subsequent growth phase. In previous work Gaussian approximation is has been used for the radius size distribution function in microgel form factor fitting^[4]. Particle radius distributions fitted using Burr type XII distribution, are shown in Figure 6. Numerical values are given in Table 1. Especially for APS-TEMED initiated batches (red histograms), the optimization routine finds slightly right tailed solutions. KPS initiated batches (blue histograms) appear to retain their polydispersity regardless of the cross-linker concentration in the batch, typically under 10 %, whereas APS-TEMED initiated batches seem to have minimum polydispersity at below 10 % between 1.9 and 5.1 mol – % BIS. It is possible that particle nucleation differs between KPS and APS-TEMED initiated batches because of different cross-linking characteristics of these systems and initiation rate, which is typically an order of magnitude higher for redox initiation^[9] in comparison to thermally decomposing initiator.

Hydrodynamic radii measured in the swollen state (dashed red and blue lines in Figure 6 for APS-TEMED and KPS initiated batches, respectively) align with the largest particle size fractions of the corresponding particle size distributions. This is to be expected for two reasons. First, correlograms could be acquired only at low q because of the fast decay of form factors. In this region the scattered intensity is dominated by the large particle size fractions due to the underlying physical process, leading to apparent hydrodynamic radii reflecting this bias. Second, hydrodynamic interactions of the particles are strongly affected by the dangling chains at the surface, increasing the apparent hydrodynamic radius further.

For selected batches particles were dried on wafer and imaged with scanning electron microscope in an effort to obtain more insight into the shape of the particle size distributions. For batches 0 and 1.9 mol – % KPS the radii of 22414 and 18390 particles were automatically counted; for batch 4.1 mol – % APS-TEMED 8787 particles were counted. Large particle counts are necessary to obtain meaningful statistics. The particle count histograms are included in Figure 6, representative examples of micrographs are shown in Figure 7.

The particle radii obtained in dry state on wafer are clearly smaller than those ob-

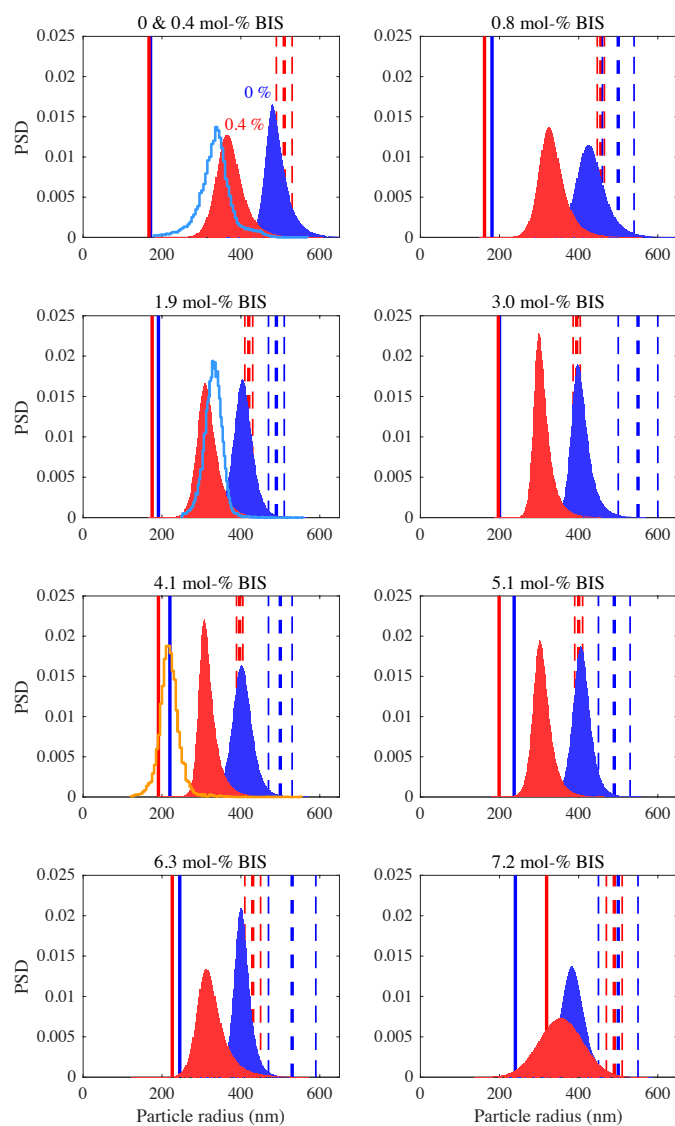


Figure 6: Particle size distributions from the fit data. Dark blue and red denote distributions from KPS and APS-TEMED initiated batches at 20 °C, respectively. Vertical solid lines with the same color coding show the mean hydrodynamic radii in the collapsed state measured by DLS at 50 °C. Dashed thick and thin lines denote hydrodynamic radii and corresponding standard deviations measured at 20 °C. Light blue and orange histograms are the results from SEM image analysis for KPS and APS-TEMED initiated batches in dry state, respectively.

Table 1: Particle size parameters for KPS and APS-TEMED (A-T) initiated batches. The KPS batches are different than those presented in the paper. Mean and PDI are the values in swollen state at 20 °C obtained from the inversion routine. Hydrodynamic radii with standard deviations were determined experimentally for all particles in collapsed state at 50 °C and for APS-TEMED initiated batches in swollen state at 20 °C. The swollen hydrodynamic radii contain significant systematic error due to the physics of the scattering process; see text for discussion.

Initiator	BIS (%)	Mean _{20°C} (nm)	PDI (%)	$R_{h,50°C}$ (nm)	$R_{h,20°C}$ (nm)
KPS	0	492	7	171 ± 2	-
KPS	0.8	432	10	181 ± 1	500 ± 40
KPS	1.9	406	7	191 ± 3	490 ± 20
KPS	3.0	407	7	200 ± 4	550 ± 50
KPS	4.1	404	7	220 ± 2	500 ± 30
KPS	5.1	408	6	237 ± 2	490 ± 40
KPS	6.3	404	6	245 ± 1	530 ± 60
KPS	7.2	386	9	240 ± 2	500 ± 50
A-T	0.4	374	10	167 ± 1	510 ± 20
A-T	0.8	334	11	162 ± 2	456 ± 9
A-T	1.9	317	9	175 ± 2	420 ± 10
A-T	3.0	309	8	197 ± 3	395 ± 9
A-T	4.1	317	8	191 ± 2	397 ± 8
A-T	5.1	308	8	199 ± 3	400 ± 10
A-T	6.3	326	12	226 ± 2	430 ± 20
A-T	7.2	356	15	319 ± 7	490 ± 20

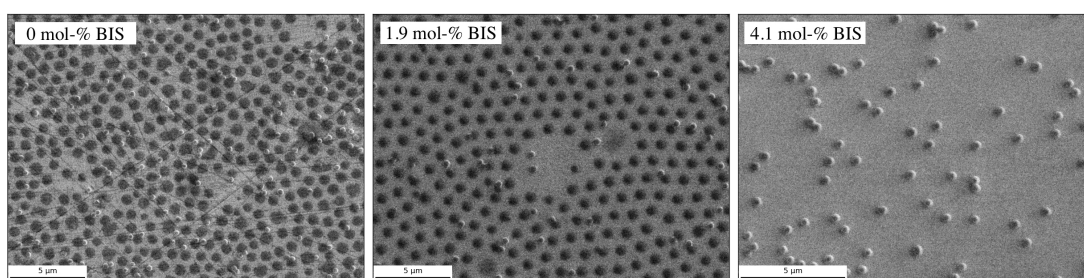


Figure 7: Scanning electron micrographs from 0 mol – % BIS KPS, 1.9 mol – % BIS KPS and 4.1 mol – % BIS APS-TEMED. In micrographs A and B contamination from the preparation is visible, but these small particles could be easily excluded from the particle counting. Low cross-linking density batches are spread on the wafer whereas 4.1 mol – % particles protrude from the substrate. Cross-link density in 0 mol – % BIS KPS is low, as the scratches in the substrate show through the particles.

tained from the fit routine at the swollen state and appear symmetric. For KPS initiated batches however, the mean dry radius is clearly far away from the collapsed hydrodynamic radius recorded at 50 °C. This discrepancy can be explained by the deformation of the microgels on the wafer: Particles with low cross-linking densities have low mechanical strength, which makes them highly deformable. The deformation of microgel particles in dry and wet states on substrate has been reported in many contexts^[10,11,12,13,14,15,16,17,18]. This can be especially expected in the case for the core-depleted particles, which lack internal support. Interaction with the substrate causes them to spread on the wafer (Figure 7, 0 and 1.9 mol – % BIS), drastically increasing the apparent radius when imaged from above. The deformation is a non-trivial non-linear process, and therefore we do not expect the particle radius distribution in the dry state on the wafer directly reflect the distribution in the swollen state.

The mean of the distribution for 4.1 mol – % APS-TEMED is in the close vicinity of the solid red line denoting the hydrodynamic radius in the collapsed state. The higher cross-linking density in this batch enhances the mechanical strength of the particles and consequently they do not deform as strongly on the wafer in the dry state^[12]. This is also visible in Figure 7, where the 4.1 mol – % APS-TEMED particles clearly protrude from the substrate. The dry state distribution also looks symmetric, as do the KPS histograms, whereas the solution obtained by the fit routine is slightly right skewed. Similar SEM histograms were obtained by von Nessen et al.^[19], with approximately 300 particles per histogram. To summarize, the experimental data shows that the distributions are monomodal and close to symmetric, but further theoretical and improved experimental work are required to settle the matter in the future. The best approach will be likely particle counting from cryo-TEM micrographs, where particle dimensions are not distorted by the interaction with substrate.

References

- [1] O Glatter. *Static Light Scattering of Large Systems*. In P. Lindner and Th. Zemb, editors, *Neutrons, X-rays and Light: Scattering Methods Applied to Soft Condensed Matter*. Amsterdam: North Holland Delta Series, 2002.
- [2] G Mie. Beitrage zur Optik trüber Medien, speziell kolloidaler Metallösungen. *Annalen der Physik*, 25:377–445, 1908.
- [3] N Sultanova and S Kasarova. Dispersion Properties of Optical Polymers. *Acta Physica Polonica- ...*, 2009.
- [4] M. Stieger, J. S. Pedersen, W. Richtering, and P. Lindner. Small-angle neutron scattering study of structural changes in temperature sensitive microgel colloids. *Journal of Chemical Physics*, 120(13):6197–6206, 2004.
- [5] Hansen, P. C. *Discrete inverse problems: insight and algorithms*. Society for Industrial and Applied Mathematics, Philadelphia, 2010.
- [6] S W Provencher. A Constrained Regularization Method For Inverting Data Represented By A Linear Algebraic or Integral Equations. *Computer Physics Communications*, 27(3):213–227, 1982.
- [7] R. Pelton. Temperature-sensitive aqueous microgels. *Advances in Colloid and Interface Science*, 85:1–33, 2000.
- [8] Otto L J Virtanen, Helmi M Ala-Mutka, and Walter Richtering. Can the Reaction Mechanism of Radical Solution Polymerization Explain the Microgel Final Particle Volume in Precipitation Polymerization of N-Isopropylacrylamide? *Macromol. Chem. Phys.*, 216(13):1431–1440, May 2015.
- [9] G. Odian. *Principles of Polymerization*. Wiley Interscience, 4th edition, 2004.
- [10] Sarah Höfl, Lothar Zitzler, Thomas Hellweg, Stephan Herminghaus, and Frieder Mugele. Volume phase transition of “smart” microgels in bulk solution and adsorbed at an interface: A combined AFM, dynamic light, and small angle neutron scattering study. *Polymer*, 48(1):245–254, January 2007.
- [11] Oya Tagit, Nikodem Tomczak, and G Julius Vancso. Probing the Morphology and Nanoscale Mechanics of Single Poly(N-isopropylacrylamide) Microgels Across the Lower-Critical-Solution Temperature by Atomic Force Microscopy. *Small*, 4(1):119–126, January 2008.
- [12] Stephan Schmidt, Hubert Motschmann, Thomas Hellweg, and Regine von Klitzing. Thermoresponsive surfaces by spin-coating of PNIPAM-co-PAA microgels: A combined AFM and ellipsometry study. *Polymer*, 49(3):749–756, February 2008.
- [13] Courtney D Sorrell and L Andrew Lyon. Deformation Controlled Assembly of Binary Microgel Thin Films. *Langmuir*, 24(14):7216–7222, July 2008.
- [14] Anna Burmistrova and Regine von Klitzing. Control of number density and swelling/shrinking behavior of P(NIPAM-AAc) particles at solid surfaces. *J. Mater. Chem.*, 20(17):3502–6, 2010.

- [15] Stefan Wellert, Yvonne Hertle, Marcel Richter, Martin Medebach, David Magerl, Weinan Wang, Bruno Demé, Aurel Radulescu, Peter Müller-Buschbaum, Thomas Hellweg, and Regine von Klitzing. Inner Structure of Adsorbed Ionic Microgel Particles. *Langmuir*, 30(24):7168–7176, June 2014.
- [16] Florian Schneider, Andreea Balaceanu, Artem Feoktystov, Vitaliy Pipich, Yaodong Wu, Jürgen Allgaier, Wim Pyckhout-Hintzen, Andrij Pich, and Gerald J Schneider. Monitoring the Internal Structure of Poly(N-vinylcaprolactam) Microgels with Variable Cross-Link Concentration. *Langmuir*, 30(50):15317–15326, December 2014.
- [17] Haylee Bachman, Ashley C Brown, Kimberly C Clarke, Kabir S Dhada, Alison Douglas, Caroline E Hansen, Emily Herman, John S Hyatt, Purva Kodlekere, Zhiyong Meng, Shalini Saxena, Mark W Spears Jr, Nicole Welsch, and L Andrew Lyon. Ultrasoft, highly deformable microgels . *Soft Matter*, 11(10):2018–2028, February 2015.
- [18] Stefan Wellert, Dikran Kesal, Sebastian Schön, Regine von Klitzing, and Kornelia Gawlitza. Ethylene Glycol-Based Microgels at Solid Surfaces: Swelling Behavior and Control of Particle Number Density. *Langmuir*, 31(7):2202–2210, February 2015.
- [19] Katja von Nessen, Matthias Karg, and Thomas Hellweg. Thermoresponsive poly-(N-isopropylmethacrylamide) microgels: Tailoring particle size by interfacial tension control. *Polymer*, 54(21):5499–5510, October 2013.